Materials Transactions, Vol. 45, No. 4 (2004) pp. 1113 to 1119
Special Issue on Frontiers of Smart Biomaterials

Tensile Deformation Behavior of Ti-Nb-Ta-Zr Biomedical Alloys*[1]

Nobuhito Sakaguch*[2], Mitsuo Niinomi and Toshikazu Akahori

Department of Production Systems Engineering, Toyohashi University of Technology, Toyohashi 441-8580, Japan

The composition of Ti-30Nb-10Ta-5Zr, which is simplified that of the Ti-29Nb-13Ta-4.6Zr alloy developed for biomedical applications, was selected, and then Nb content in the basic composition was varied from 20 to 35%. The deformation mechanisms of such Ti-Nb-Ta-Zr system alloys were investigated by loading-unloading tensile tests and characterizing deformed microstructures. The behavior of unloading and reloading of the stress-strain curves up to strain about 2% of Ti-20Nb-10Ta-5Zr and Ti-25Nb-10Ta-5Zr alloys is similar to that obtained in metastable β type titanium alloys where the stress induced martensite transformation occurs. This indicates that the stress and strain induced martensite transformation occurred in these alloys. Furthermore, the elastic deformation of Ti-30Nb-10Ta-5Zr alloy disobeys Hooke's law. However, the behavior of stress or strain-induced martensite transformation does not recognized in the stress-strain curve up to strain about 2% of this alloy. The main deformation mechanism up to fracture of Ti-20Nb-10Ta-5Zr alloy, Ti-25Nb-10Ta-5Zr alloy and Ti-35Nb-10Ta-5Zr alloy is identified as the deformation - induced martensite transformation of β phase to α'' phase, deformation-induced martensite transformation of β phase to α'' phase and deformation twin, and slip, respectively. The deformation mechanisms for Ti-30Nb-10Ta-5Zr alloy are not explained by slip, deformation twining and deformation-induced martensite transformation. However, the super elastic behavior observed in this alloy is expected to occur without deformation-induced martensite transformation.

(Received November 19, 2003; Accepted February 12, 2004)

Keywords: *titanium alloy, super elastic deformation, shape memory biomaterial, powder metallurgy*

1. Introduction

Recently, titanium and its alloys have been widely used for biomaterials due to their high biocompatibility. Initially, titanium alloys made for general structural materials have been used for biomaterials. However, from the point of view of safety, the uses of the general structural titanium alloys containing toxic elements like V and so on have become serious problems. Therefore, new titanium alloys such as Ti-13Nb-13Zr alloy[1)] (In this study, all alloy compositions are written by mass%), Ti-35Nb-5Ta-7Zr alloy[2)] and Ti-29Nb-13Ta-4.6Zr alloy[3,4)] etc. composed of non-toxic elements like Nb, Ta, and Zr have been developed for biomaterials for next generation.

However, the number of reports on the effects of alloying elements on various properties of the Ti-Nb-Ta-Zr system alloys is very small so far.[5–9)] Therefore, the authors investigated the effect of Nb on the microstructures and mechanical properties of the Ti-Nb-Ta-Zr system alloys. In that case, the chemical composition of Ti-30Nb-10Ta-5Zr alloy, which is simplified that of the Ti-29Nb-13Ta-4.6Zr alloy, was selected as a base, and the Nb content of it was varied from 0 through 40 mass% by eight levels (0, 10, 15, 20, 25, 30, 35 and 40 mass%). In the Ti-Nb-Ta-Zr system alloys, the stress induced martensite α'' phase has been recognized in the deformed microstructures of the Ti-20Nb-10Ta-5Zr alloy and Ti-25Nb-10Ta-5Zr alloy after tensile tests.

Generally, deformation mechanism of β phase alters with the change in the stability of β phase.[10–12)] The main deformation mechanisms of β phase are as follows:

(1) Slip.
(2) Twining.
(3) Stress- or strain-induced martensite transformation of β phase to α'' phase.

High ductility is obtained by combination of these deformation mechanisms.

In Ti-Nb-Sn system alloys,[13)] Ti-Sc-Mo system alloys[14)] and Ti-Mo-Ag system alloys,[15)] shape memory effect and super elastic behavior have been reported. Very recently, the shape memory effect has been also reported in Ti-20Nb-10Ta-5Zr alloy.[16)]

However, the deformation behavior of Ti-Nb-Ta-Zr system alloys has not been clear yet. Therefore, the deformation behavior of Ti-Nb-Ta-Zr system alloys was investigated in this study.

2. Experimental Procedures

Ti-30Nb-10Ta-5Zr alloy ($TNTZ_{30}$), which is simplified Ti-29Nb-13Ta-4.6Zr alloy developed for biomaterials, was selected as the basic alloy composition. The Nb content of this alloy was varied by 3 levels of 20 mass% ($TNTZ_{20}$), 25 mass% ($TNTZ_{25}$), and 35 mass% ($TNTZ_{35}$).

Blended elemental powder metallurgy method was applied to fabricate these alloys. Mean particle size and purity of each element powder used in this study were under 45 μm and over 99.8%, respectively. These powders were mixed and pressed to form green products with a diameter of 40 mm and a length of about 100 mm by a cold isostatic pressing machine. Green products were then sintered at 1573 K for 57.3 ks in a vacuum of about 1.33×10^{-3} Pa. Subsequently, they were forged and swaged at 1223 K to make bars with a diameter of 10 mm. Finally, the swaged bars were subjected to heat treatment at 1123 K for 1.8 ks followed by air cooling to remove residual stress resulting from hot forging and hot swaging. Table 1 shows chemical composition of each Ti-Nb-Ta-Zr system alloy.

The microstructures of Ti-Nb-Ta-Zr system alloys were observed using an optical microscope and a transmission electron microscope (TEM). Diffraction pattern analyses using a TEM and X-ray diffraction analysis (XRD) using a Cu-Kα tube were carried out in order to identify the phases

*[1]This Paper was Presented at the Spring Meeting of the Japan Institute of Metals, held in Chiba, on March 28, 2003
*[2]Graduate Student, Toyohashi University of Technology

Table 1 Chemical composition of each Ti-Nb-Ta-Zr system alloy.

	$TNTZ_{20}$	$TNTZ_{25}$	$TNTZ_{30}$	$TNTZ_{35}$
Ti	bal.	bal.	bal.	bal.
Nb	19.4	24.9	29.4	35.0
Ta	10.2	9.94	10.4	9.96
Zr	4.76	4.62	4.80	4.53
O	0.22	0.23	0.23	0.24

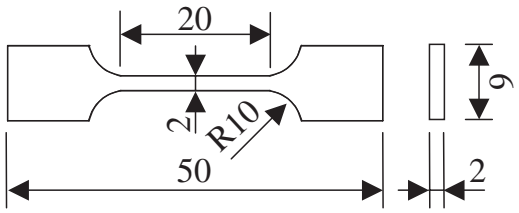

Fig. 1 Schematic drawing of specimens for loading–unloading tensile tests in mm.

constituent of the Ti-Nb-Ta-Zr system alloys.

Loading–unloading tensile tests were carried out using an Instron type testing machine at a crosshead speed of $8.33 \times 10^{-6}\,ms^{-1}$ in air at room temperature. The load was detected by a load-cell in the machine. The strain was measured by both strain gage attached directly to the specimen and movement of crosshead. Figure 1 shows the geometry of the specimens used for loading–unloading tensile tests. The crosshead was stopped at strains of 1.3%, 2.0% and 3.0%, and then the load was released after reaching each target value of strain. Finally, the specimen was loaded to fracture.

The vicinities of the fracture surfaces of specimens were observed using a scanning electron microscope (SEM), and subsequently, analyzed by XRD using a Cu-Kα tube in order to identify the deformed structures. Furthermore, the dog bone type specimens of Ti-Nb-Ta-Zr alloys, as shown in Fig. 2, were fractured by tensile tests under the same testing machine and crosshead speed as those of loading–unloading tensile tests. During tensile test the crosshead was not stopped. Subsequently, the specimens for TEM observations were made from the parallel parts of fractured dog bone type specimens.

3. Results and Discussion

3.1 Microstructures

Figure 3 shows optical micrographs of Ti-Nb-Ta-Zr system alloys. The micrograph of each Ti-Nb-Ta-Zr system alloy shows equiaxed grains. The mean grain diameter of each Ti-Nb-Ta-Zr system alloy was tabulated in Table 2.

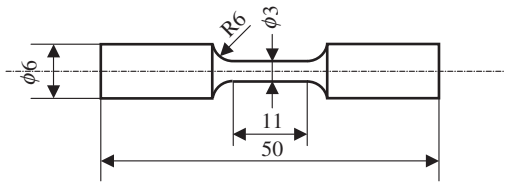

Fig. 2 Schematic drawing of dog born type specimens for tensile tests in mm.

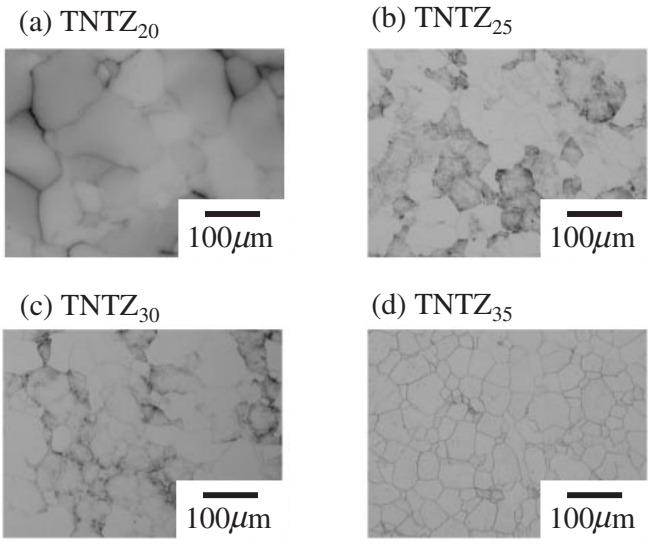

Fig. 3 Optical micrograph of each Ti-Nb-Ta-Zr system alloy: (a) $TNTZ_{20}$, (b) $TNTZ_{25}$, (c) $TNTZ_{30}$ and (d) $TNTZ_{35}$.

Table 2 Mean grain diameter of each Ti-Nb-Ta-Zr system alloy.

$TNTZ_{20}$	$TNTZ_{25}$	$TNTZ_{30}$	$TNTZ_{35}$
87.4	57.8	62.3	44.1

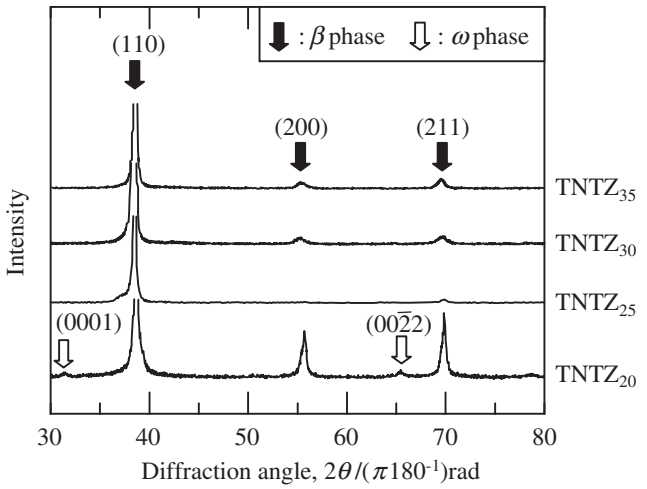

Fig. 4 X-ray diffraction pattern of each Ti-Nb-Ta-Zr system alloy.

Figure 4 shows XRD profiles of Ti-Nb-Ta-Zr system alloys. The XRD profiles of $TNTZ_{25}$, $TNTZ_{30}$ and $TNTZ_{35}$ show the peaks of single β phase. Only the XRD profile of $TNTZ_{20}$ shows the peaks of ω phase along with those of β phase.

Figures 5 and 6 show TEM dark field images, diffraction patterns and key diagrams of $TNTZ_{20}$ and $TNTZ_{25}$, respectively. Fine grains of ω phase are recognized in dark field image of $TNTZ_{20}$ (Fig. 5(a)). The diffraction pattern of $TNTZ_{25}$ clearly shows the spots corresponding to the ω phase with those of the β phase (Fig. 6(a)). However, the morphology of ω phase is not able to be identified. The

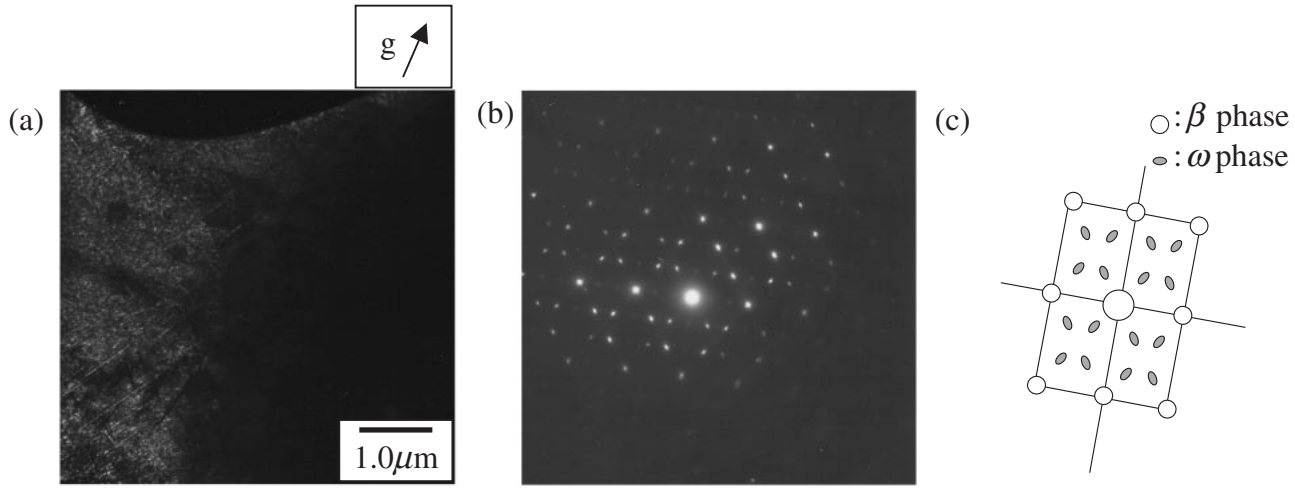

Fig. 5 TEM micrographs of $TNTZ_{20}$: (a) dark field image, (b) diffraction pattern and (c) key diagram. Beam parallel to $[011]_\beta$.

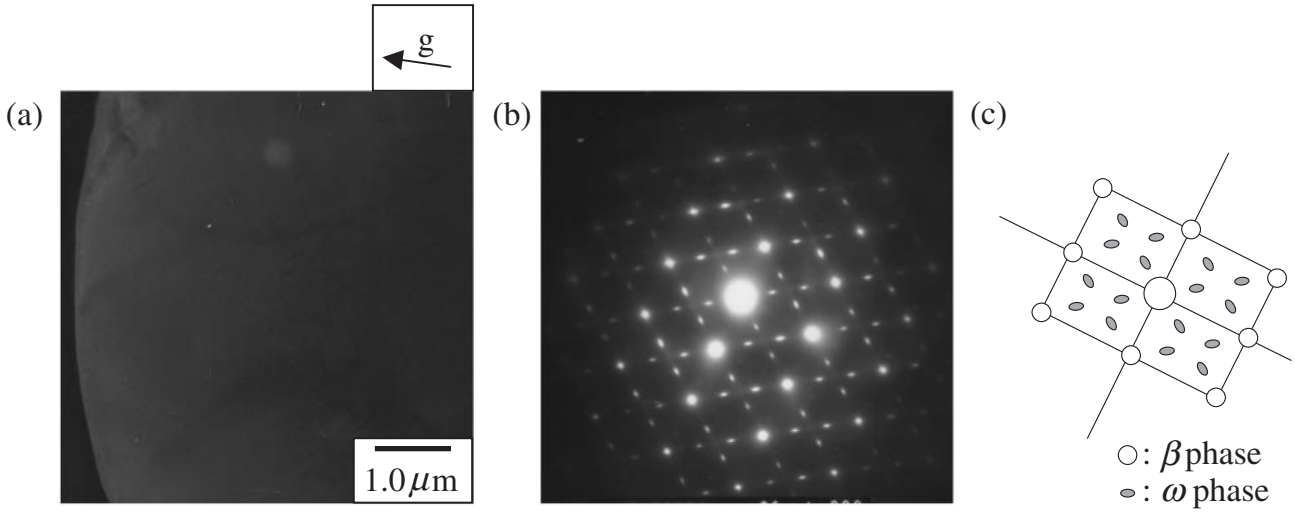

Fig. 6 TEM micrographs of $TNTZ_{25}$: (a) dark field image, (b) diffraction pattern and (c) key diagram. Beam parallel to $[011]_\beta$.

XRD profile of $TNTZ_{25}$ does not show peaks of ω phase (Fig. 4). Therefore, it is considered that the size and volume fraction of ω phases in $TNTZ_{25}$ are extremely small. These ω phases observed in $TNTZ_{20}$ and $TNTZ_{25}$ were able to be diminished by water quenching after final heat treatment of manufacturing process. Therefore, it is considered that these ω phases are isothermal ω formed during cooling. It was found that TEM micrographs of $TNTZ_{30}$ and $TNTZ_{35}$ do not show the diffraction patterns of ω phase except for those of β phase.

3.2 Tensile deformation behavior up to strain about 2%

Figure 7 shows stress-strain curve up to strain about 2% obtained from loading - unloading tensile test of each Ti-Nb-Ta-Zr system alloy. During first loading, the stress proportionally increases with increasing strain in $TNTZ_{20}$ (Fig. 7(a)). This curve shows a yielding point at a strain about 0.9%. Then, the strain of this curve increases under constant stress. In the unloading from a strain of 1.3%, this curve shows a non-liner reversion. During second loading, the stress increases with increasing the strain. This curve clearly shows two gradients.

The stress-strain curve of $TNTZ_{25}$ (Fig. 7(b)) shows a yielding point at the strain of about 0.9% as same as that of $TNTZ_{20}$. However, the yield stress of $TNTZ_{25}$ is about 200 MPa lower than that of $TNTZ_{20}$. These yield stresses are in accordance with the former report by authors.[5] Furthermore, the behavior of unloading and second loading of $TNTZ_{25}$ have similar shape to that of $TNTZ_{20}$. However, the difference of the gradients of loading curve during second loading is larger than that of $TNTZ_{20}$.

The behavior of unloading and reloading of the stress–strain curves of $TNTZ_{20}$ and $TNTZ_{25}$ is similar to that obtained in metastable β type titanium alloys where the stress induced martensite transformation occurs.[11,12] This indicates that the stress and strain induced martensite transformation occurred in $TNTZ_{20}$ and $TNTZ_{25}$.

On the other hand, the loading curves and the unloading curves of $TNTZ_{30}$ (Fig. 7(c)) do not show liner behavior. Furthermore, these curves trace the same line. The loading curves and unloading curves of $TNTZ_{35}$ (Fig. 7(d)) show liner behavior, and have same gradient. In general, the elastic

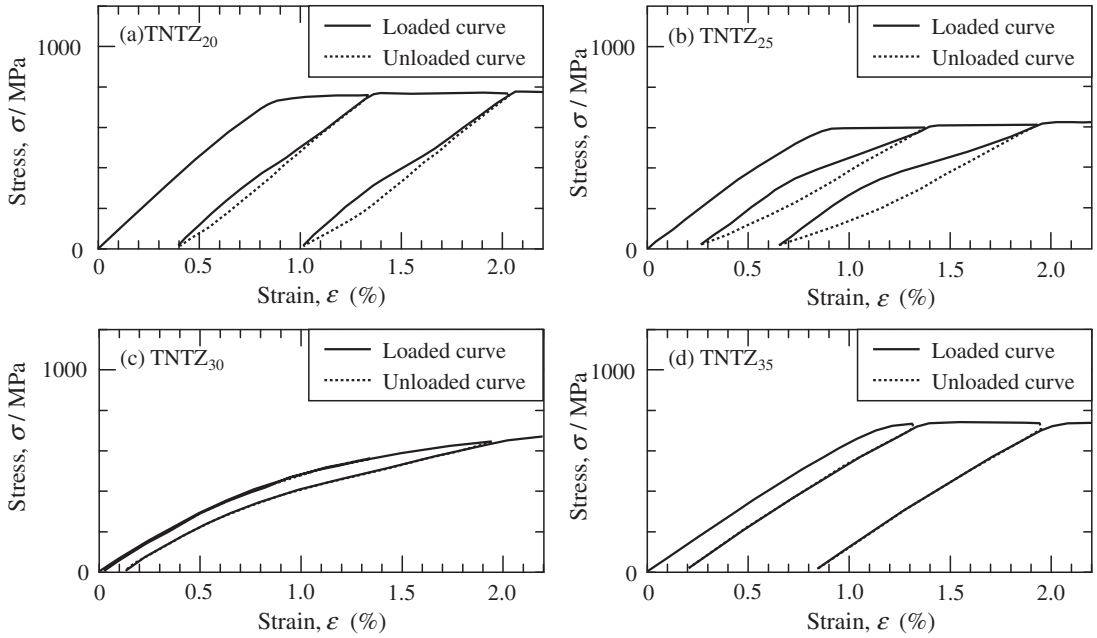

Fig. 7 Tensile loading–unloading stress-strain curve of each Ti-Nb-Ta-Zr system alloy: (a) $TNTZ_{20}$, (b) $TNTZ_{25}$, (c) $TNTZ_{30}$ and (d) $TNTZ_{35}$.

deformation of general structural metallic material obeys with Hooke's law. Therefore, the stress proportionally increases with increasing strain during elastic deformation region. The stress-strain curve of $TNTZ_{35}$ accords with Hooke's law. However, the stress-strain curve of $TNTZ_{30}$ is different from that of general structural metallic material. This curve shows the elastic–plastic deformation behavior. Therefore, the elastic deformation of $TNTZ_{30}$ disobeys Hooke's law. Furthermore, the stress-strain curve of $TNTZ_{30}$ does not show the behavior relating to the deformation induced martensite transformations, which are recognized in $TNTZ_{20}$ and $TNTZ_{25}$.

Figure 8 shows the relationship between the total strain and the elastic strain of each Ti-Nb-Ta-Zr system alloy. The elastic strain of $TNTZ_{35}$ is almost independent of change in the total strain. On the other hand, the elastic strains of $TNTZ_{20}$, $TNTZ_{25}$ and $TNTZ_{30}$ increase with increasing the total strains. In particular, this trend is remarkable in $TNTZ_{30}$. In general, the elastic strain is able to be estimated by following equation:

$$\varepsilon_e = \frac{\sigma}{E} \tag{1}$$

Therefore, the elastic strain is equal to the total strain in elastic deformation region. The trends of the elastic strains increasing with the total strain observed in $TNTZ_{20}$ and $TNTZ_{25}$ are explained by increasing the amount of deformation induced martensite transformation and its reversion. However, as stated above, the behavior of stress or strain-induced martensite transformation does not recognized in the stress-strain curve of $TNTZ_{30}$. Therefore, the behavior of $TNTZ_{30}$ is not able to be explained by increasing the amount of deformation induced martensite transformation and its reversion.

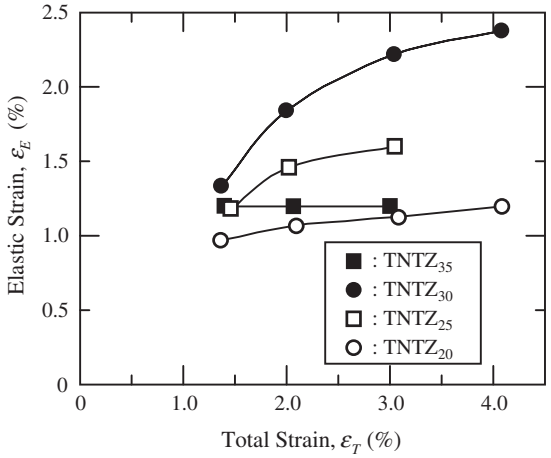

Fig. 8 Relationship between total strain, ε_T, and elastic strain, ε_E, of each Ti-Nb-Ta-Zr system alloy.

The strain recovery behavior due to the deformation induced martensite transformation in $TNTZ_{20}$ and $TNTZ_{25}$ is similar to the super elastic behavior and shape memory behavior reported for the Ti-Nb-Sn system alloys,[13] Ti-Sc-Mo system alloys[14] and Ti-Mo-Ag system alloys.[15] Therefore, the super elastic behavior and shape memory behavior are expected to occur in $TNTZ_{20}$ and $TNTZ_{25}$. On the other hand, the strain recovery of $TNTZ_{30}$ is greater than those of $TNTZ_{20}$ and $TNTZ_{25}$. Therefore, the super elastic behavior observed in $TNTZ_{30}$ is expected to occur without deformation induced martensite transformation.

3.3 Tensile deformation behavior up to fracture

3.3.1 Stress-strain curves up to fracture

Figure 9 shows stress-strain curve obtained by tensile test up to fracture of each Ti-Nb-Ta-Zr system alloy. Each stress-strain curve shows different shape. In particular, it is clear that the stress-strain curve of $TNTZ_{25}$ shows the lowest yield stress and the greatest elongation. Furthermore, the shape of

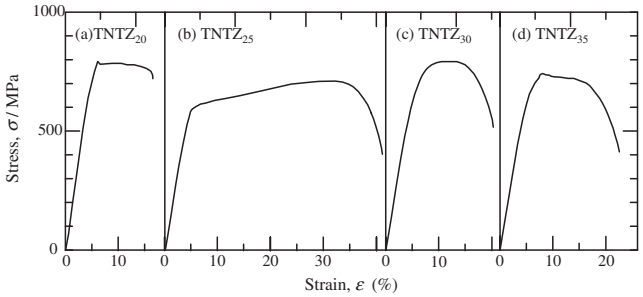

Fig. 9 Tensile stress-strain curve of each Ti-Nb-Ta-Zr system alloy: (a) $TNTZ_{20}$, (b) $TNTZ_{25}$, (c) $TNTZ_{30}$ and (d) $TNTZ_{35}$.

this stress-strain curve is different shape from that of $TNTZ_{20}$ which shows the same behavior of unloading and second loading in Fig. 7. Therefore, Ti-Nb-Ta-Zr system alloys in this study have different deformation mechanisms up to fracture, even if they show same behavior up to strain about 2%.

3.3.2 Deformed microstructures

Figure 10 shows SEM micrograph taken from a vicinity of fracture surface of each Ti-Nb-Ta-Zr system alloy. There are a number of lines near the fracture surfaces of $TNTZ_{20}$ and $TNTZ_{25}$. The morphology of the lines is very similar to that formed during deformation-induced martensite transformation of β phase to α'' phase.[17] However, these lines are not recognized in $TNTZ_{30}$ and $TNTZ_{35}$.

Figures 11, 12 and 13 show TEM bright field images, diffraction patterns and key diagrams of deformed microstructures obtained from tensile tests of $TNTZ_{20}$, $TNTZ_{25}$ and $TNTZ_{30}$, respectively. The deformed microstructures of $TNTZ_{20}$ and $TNTZ_{25}$ show ellipse or platelike phases, as shown in Fig. 11(a) and Fig. 12(a), whose shapes are similar to those of the deformation twins[17,18] or deformation-induced martensite α'' phases.[19] Both diffraction patterns taken from $TNTZ_{20}$ and $TNTZ_{25}$ consist of several diffraction patterns of β phases. However, the diffraction pattern of $TNTZ_{20}$ does not have the relation to twin (Fig. 11(b)). On the other hand, the diffraction pattern of $TNTZ_{25}$ shows a relation to twin, as shown in the key diagram (Fig. 12(c)). This relation to twin is one of $\{112\}\langle 111\rangle$ that have been identified in usual structural metallic materials with body center cubic structure. Therefore, the deformation mechanism up to fracture of $TNTZ_{25}$ is identified different from that of $TNTZ_{20}$, although they show the same behavior up to strain about 2%. On the other hand, ellipse or platelike phases were not recognized in $TNTZ_{30}$ and $TNTZ_{35}$. In particular, a large number of tangled dislocations are recognized in deformed structure of $TNTZ_{30}$ (Fig. 13(a)). The relation to twin shown in Fig. 13(b) is rarely recognized in $TNTZ_{30}$.

Figure 14 shows XRD profile obtained near the fracture surface of each Ti-Nb-Ta-Zr system alloy after tensile test. The peaks of α'' phases that were not recognized in XRD profiles of specimen surfaces before tensile tests (Fig. 4) are recognized on the specimen surface near the fracture surfaces of $TNTZ_{20}$ and $TNTZ_{25}$. Therefore, it is considered that α''

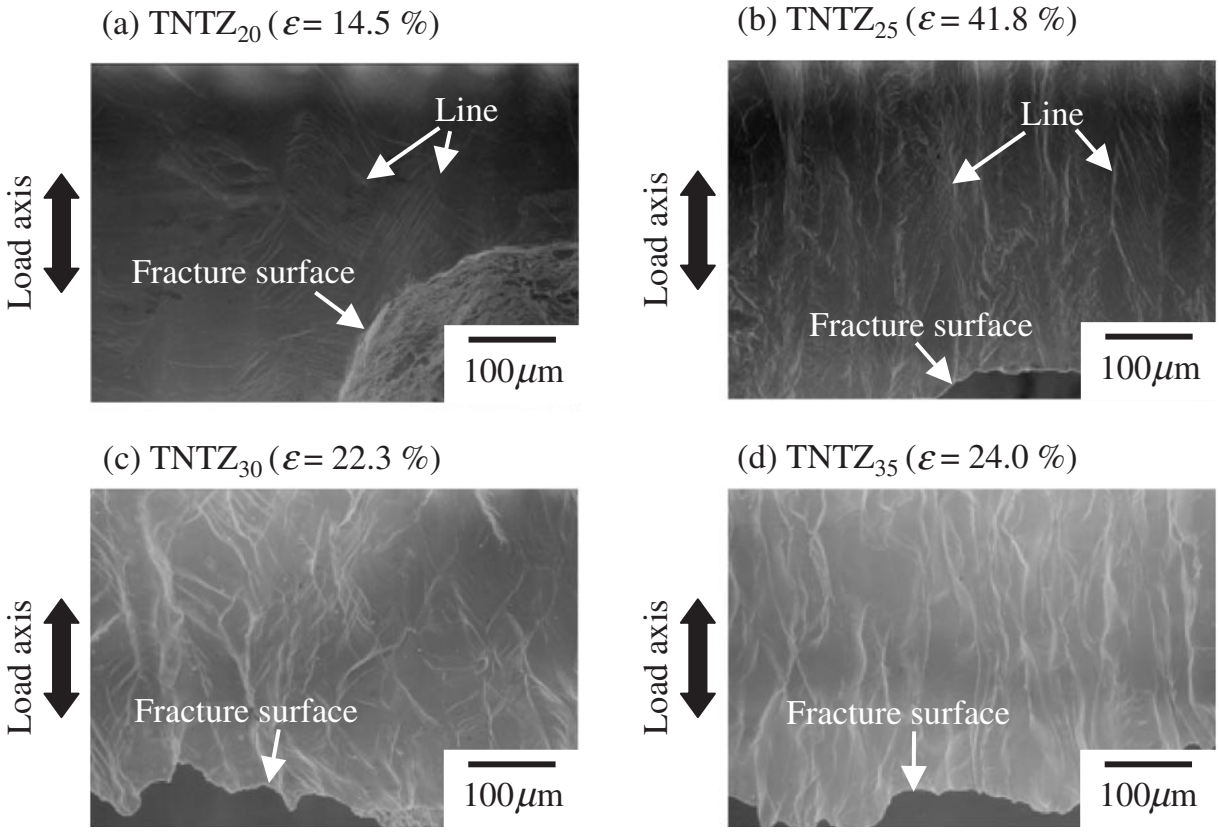

Fig. 10 SEM image taken near the fracture surface of each Ti-Nb-Ta-Zr system alloy after tensile test: (a) $TNTZ_{20}$, (b) $TNTZ_{25}$, (c) $TNTZ_{30}$ and (d) $TNTZ_{35}$.

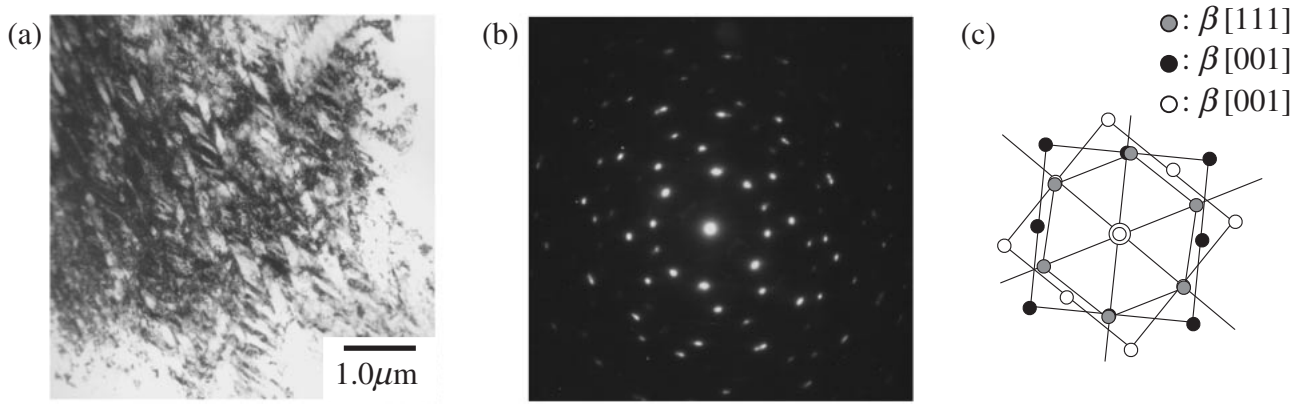

Fig. 11 TEM micrographs obtained near the fracture surface of $TNTZ_{20}$ ($\varepsilon = 16.5\%$) after tensile test: (a) bright field image, (b) diffraction pattern and (c) key diagram.

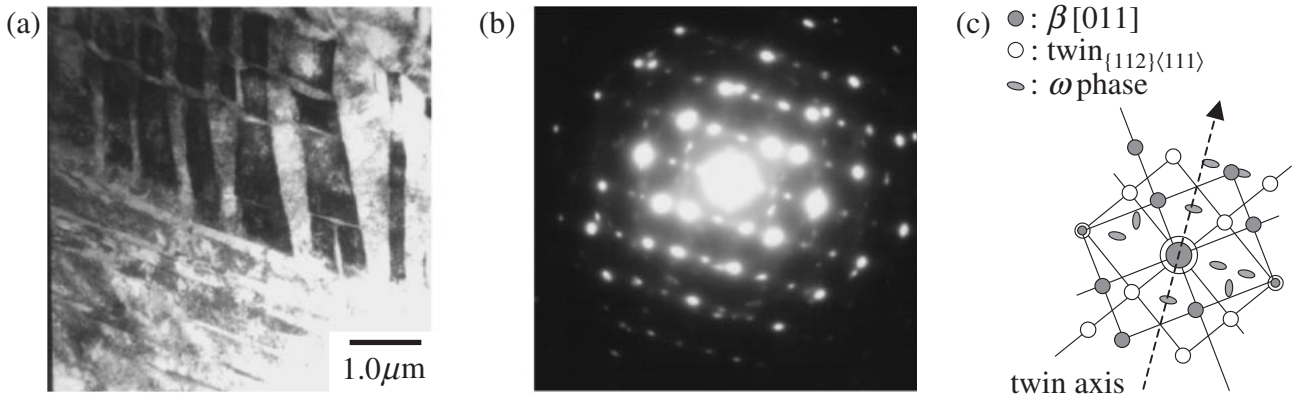

Fig. 12 TEM micrographs obtained near the fracture surface of $TNTZ_{25}$ ($\varepsilon = 40.4\%$) after tensile test: (a) bright field image, (b) diffraction pattern and (c) key diagram.

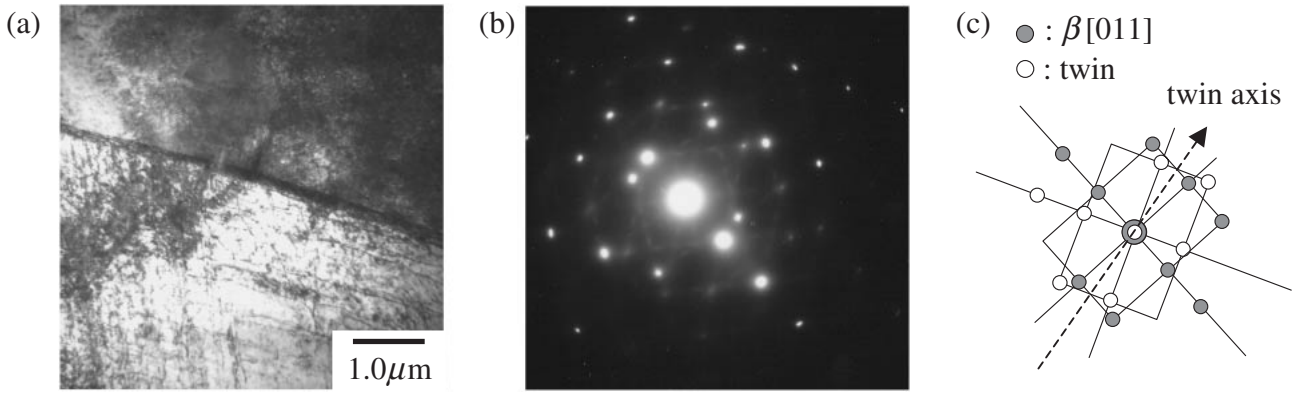

Fig. 13 TEM micrographs obtained near the fracture surface of $TNTZ_{30}$ ($\varepsilon = 18.6\%$) after tensile test: (a) bright field image, (b) diffraction pattern and (c) key diagram.

phase was formed during deformation. The peaks of α'' phases are not recognized in XRD profiles obtained near the fracture surfaces of $TNTZ_{30}$ and $TNTZ_{35}$. The peaks of β phase in XRD profile obtained near the fracture surface of $TNTZ_{30}$ shift to a lower angle than those before tensile test. Therefore, it is considered that the lattice of β phase has been distorted in $TNTZ_{30}$.

From the results of the TEM observations and XRD analyses on deformed structures after tensile tests, the main deformation mechanism up to fracture of $TNTZ_{20}$, $TNTZ_{25}$ and $TNTZ_{35}$ is identified the deformation — induced martensite transformation of β phase to α'' phase, deformation-induced martensite transformation of β phase to α'' phase and deformation twin, and slip, respectively. As stated in introduction, deformation mechanism of β phase alters with the change in the stability of β phase.[10–12] This change

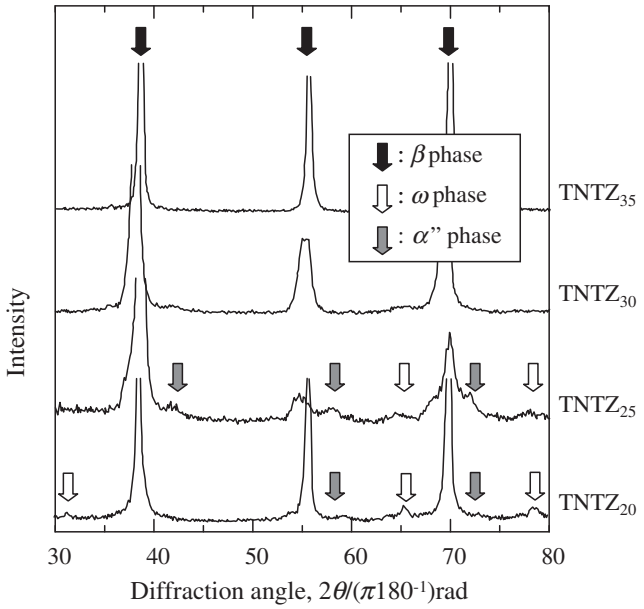

Fig. 14 X-ray diffraction patterns obtained near the fracture surface after tensile test: (a) $TNTZ_{20}$, (b) $TNTZ_{25}$, (c) $TNTZ_{30}$ and (d) $TNTZ_{35}$.

of deformation mechanism with changing Nb composition in $TNTZ_{20}$, $TNTZ_{25}$ and $TNTZ_{35}$ is in accordance with the tendency by the stability of β phase.

However, in the present state, the deformation mechanisms for $TNTZ_{30}$ are not explained by slip, deformation twining and deformation-induced martensite transformation, and a further investigation is necessary to make it clear.

4. Conclusions

The deformation behavior of Ti-Nb-Ta-Zr system alloys with different Nb contents was investigated in this study. The following results were obtained.

(1) The behavior of unloading and reloading of the stress-strain curves up to strain about 2% of $TNTZ_{20}$ and $TNTZ_{25}$ are similar to that obtained in metastable β type titanium alloys where the stress induced martensite transformation occurs. It is indicated that the stress and strain induced martensite transformation occurred in these alloys.

(2) The elastic deformation of $TNTZ_{30}$ disobeys Hooke's law. However, the behavior of stress or strain-induced martensite transformation does not recognized in the stress-strain curve up to strain about 2% of this alloy.

(3) The main deformation mechanism up to fracture of $TNTZ_{20}$, $TNTZ_{25}$ and $TNTZ_{35}$ is identified the deformation-induced martensite transformation of β phase to α'' phase, deformation-induced martensite transformation of β phase to α'' phase and deformation twin, and slip, respectively.

(4) The deformation mechanisms for $TNTZ_{30}$ are not explained by slip, deformation twining and deformation-induced martensite transformation. However, the super elastic behavior observed in $TNTZ_{30}$ is expected to occur without deformation-induced martensite transformation.

Acknowledgements

The authors would like to thank Dr. T. Saito, Dr. T. Furuta, Dr. K. Nishino, Dr. J. H. Hwang and Dr. S. Kuramoto (Toyota Central R&D Labs., Inc., Nagakute, Japan) for helping in manufacturing ingots and analyzing chemical compositions.

REFERENCES

1) M. Geetha, A. K. Singh, K. Muraleedharan, A. K. Gogia and R. Asokamani: J. Alloy Comp. **329** (2001) 264–271.
2) T. Ahmed, M. Long, J. Slivestri, C. Ruiz and H. J. Rack: Proc. Titanium '95 (Inst. Metals, 1996) pp. 1760–1767.
3) D. Kuroda, M. Niinomi, M. Morinaga, Y. Kato and T. Yashiro: Mater. Sci. Eng. **A243** (1998) 244–249.
4) D. Kuroda, M. Niinomi, H. Fukui, A. Suzuki and J. Hasegawa: Tetsu-to-Hagane **86** (2000) 610–616.
5) N. Sakaguchi, M. Niinomi, T. Akahori, T. Saito and T. Furuta: J. Japan Inst. Metals **67** (2003) 681–687.
6) N. Sakaguchi, M. Niinomi, T. Akahori, T. Saito and T. Furuta: Proc. of Int. Conf. on Advanced Technology in Experimental Mechanics 2003, (The Japan Society of Mechanical Engineering 2003) CD-ROM.
7) N. Sakaguchi, M. Niinomi, T. Akahori, T. Saito and T. Furuta: Abstracts of 104th Spring Meeting of the Japan Institute of Light Metals (2003) pp. 75–76.
8) S. Yoshitani, M. Niinomi, D. Kuroda, K. Fukunaga, T. Saito and T. Furuta: Proceedings of 2000 Powder Metallurgy World Congress, (The Japan Society of Powder Metallurgy and the Japan Powder Metallurgy Association, 2000) pp. 1085–1088.
9) S. Li, Y. Hao, Y. Cui and M. Niinomi: Mater. Trans. **43** (2002) 2964–2969.
10) S. Hanada, M. Ozeki and O. Izumi: Metall. Trans. A **16A** (1985) 789–795.
11) T. Grosdidier and M. J. Philippe: Mater. Sci. Eng. **A291** (2000) 218–223.
12) T. Grosdidier, Y. Combres, E. Gautier and M. J. Philippe: Metall. Mater. Trans. A **31A** (2000) 1095–1106.
13) E. Takahashi, S. Watanabe and S. Hanada: Collected Abstracts of the 2003 Spring Meeting of the Japan Inst. Metals (2003) pp. 135.
14) T. Maejima, T. Eto, H. Uchiyama, K. Yamauchi and M. Nishida: Collected Abstracts of the 2003 Spring Meeting of the Japan Inst. Metals (2003) pp. 134.
15) T. Maejima, T. Eto, H. Uchiyama, K. Yamauchi and M. Nishida: Collected Abstracts of the 2003 Spring Meeting of the Japan Inst. Metals (2003) pp. 135.
16) K. Ikeda, A. Sugimoto, Y. Shintaklu and M. Niimomi: Abstracts of 104th Spring Meeting of the Japan Institute of Light Metals (2003) pp. 409–410.
17) M. Oka and Y. Taniguchi: J. Japan Inst. Metals **42** (1978) 814–820.
18) M. Hida, E. Sukedai, Y. Yokohari and A. Nakagawa: J. Japan Inst. Metals **44** (1980) 436–442.
19) Y. Ohmori, T. Ogo, K. Nakai and S. Kobayashi: Mater. Sci. Eng. **A321** (2001) 182–188.